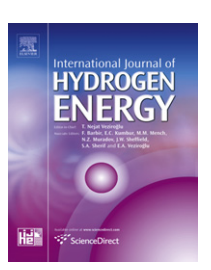


Available online at www.sciencedirect.com

## SciVerse ScienceDirect

journal homepage: www.elsevier.com/locate/he



# Microstructure and reactivity effects on the performance of $Nd_2NiO_{4+\delta}$ oxygen electrode on $Ce_{0.9}Gd_{0.1}O_{1.95}$ electrolyte

A. Montenegro-Hernández a,b, L. Mogni a,b, A. Caneiro a,b,c,\*

- <sup>a</sup> Instituto Balseiro, Centro Atómico Bariloche, 8400 San Carlos de Bariloche, Río Negro, Argentina
- <sup>b</sup> Consejo Nacional de Investigaciones Científicas y Técnicas CONICET, Argentina

#### ARTICLE INFO

Article history:
Received 23 April 2012
Received in revised form
10 September 2012
Accepted 11 September 2012
Available online 8 October 2012

Keywords:
Fuel cells
SOFC cathode
Nickelates
Oxygen reduction reaction

#### ABSTRACT

The effect of electrode microstructure on the electrochemical behavior of symmetrical Nd<sub>2</sub>NiO<sub>4+ $\delta$ </sub>/Ce<sub>0.9</sub>Gd<sub>0.1</sub>O<sub>1.95</sub>/Nd<sub>2</sub>NiO<sub>4+ $\delta$ </sub> cells was studied by Electrochemical Impedance Spectroscopy as a function of temperature (500 < T < 750 °C) and oxygen partial pressure (10<sup>-4</sup> < pO<sub>2</sub> < 1 atm). Nd<sub>2</sub>NiO<sub>4+ $\delta$ </sub> powders were synthesized by Solid State Reaction, HMTA and Citrates. The samples observed by Scanning Electron Microscopy presented very different microstructures. Three characteristic processes were distinguished at high, medium and low frequency. High frequency contribution was attributed to oxygen ion transfer electrode/electrolyte. Medium frequency contribution was related to oxygen interstitial bulk diffusion and oxygen incorporation in those cases in which the surface of small particles is affected by chemical reactivity with the electrolyte. The low frequency contribution was attributed to dissociative adsorption for electrodes with small particle sizes and high porosity, and a co-limited process of adsorption and gas diffusion for an electrode with dense microstructure and low porosity.

Copyright © 2012, Hydrogen Energy Publications, LLC. Published by Elsevier Ltd. All rights reserved.

#### 1. Introduction

In the last years, the requirements of efficient systems for energy conversion and the choice of  $H_2$  as energy vector, have focussed the research on new materials for these applications. Solid Oxide Cells (SOCs) used in fuel cell mode (SOFC) for electrochemical energy conversion or as electrolyzers (SOECs) for producing clean  $H_2$  are good examples of interesting applications in this field [1–3].

 ${
m Nd_2NiO_{4+\delta}}$  (NNO) has been recently reported as potential oxygen electrode for both SOC applications, SOFC and SOEC, due to its reversibility in the reduction reaction of O<sub>2</sub> [4–7]. These authors found that cells using NNO electrodes display

current densities 3 or 4 times higher than similar cells tested with conventional  $La_{0.8}Sr_{0.2}MnO_3$  (LSM) oxygen electrodes. A possible explanation of this feature could be the presence of interstitial oxygen which promotes both ionic and electronic conductivities [4–7]. On the contrary, LSM perovskite materials are practically pure electronic conductors since they do not have enough lattice oxygen defects to promote ionic conductivity under oxidizing atmospheres.

NNO is a mixed conductor with the  $K_2NiF_4$  type structure belonging to the first order Ruddlesden–Popper family  $Ln_2NiO_{4+\delta}$ , where Ln is a lanthanide cation such as La, Pr or Nd. The crystal structure of  $Ln_2NiO_{4+\delta}$  consists of alternating LnO rock salt and  $LnNiO_3$  perovskite layers [8,9]. Interstitial

<sup>&</sup>lt;sup>c</sup> Comisión Nacional de Energía Atómica CNEA, Argentina

<sup>\*</sup> Corresponding author. Instituto Balseiro, Centro Atómico Bariloche, 8400 San Carlos de Bariloche, Río Negro, Argentina. Tel.: +54 2944 445274; fax: +54 2944 445299.

E-mail address: caneiro@cab.cnea.gov.ar (A. Caneiro).

oxygen can be accommodated into the rock salt layers, promoting ionic [10-12] and p-type electronic conductivities [13].

NNO oxide fulfills some requirements for SOCs oxygen electrodes as for example: high values of oxygen exchange and oxygen diffusion coefficients [10–12], high electronic conductivity [13], and thermal expansion coefficients (TEC) similar to  $Zr_xY_{1-x}O_{(x+3)/2}$  (YSZ) and  $Ce_xGd_{1-x}O_{(x+3)/2}$  (CGO) electrolytes [13]. However, one disadvantage of this material is the reactivity with electrolytes at high temperatures [14,15]. Both reactivity and electrode performance strongly depend on the microstructure [14,16,17]. Nevertheless, to the best of our knowledge, no studies have been performed on the relation between the oxygen reduction reactions (ORR) mechanisms and microstructure for NNO electrodes deposited on CGO electrolytes. This information is essential for a better design of electrode materials.

In this work, NNO electrode material has been obtained by three different synthesis methods, each of them yielding a characteristic microstructure. Electrochemical Impedance Spectroscopy (EIS) was carried out as a function of both temperature (T) and oxygen partial pressure ( $pO_2$ ) in order to study the oxygen electrode reaction of porous NNO deposited on dense CGO electrolytes. With the obtained information, a reaction mechanism related to microstructural and reactivity effects was proposed.

## 2. Experimental

NNO powders were synthesized by three different methods. The first one named "HMTA method" [18] uses Nd<sub>2</sub>O<sub>3</sub> and Ni(CH<sub>3</sub>COO)<sub>2</sub>·H<sub>2</sub>O, with analytic grade as precursors. Stoichiometric amounts of precursors were dissolved in acetic acid with hexamethylenetetramine (HMTA) and acetylacetone, in a (ligand:metal) 3:1 molar ratio. The solution was refluxed and heated until a brown gel was obtained. This gel was fired at 400 °C and finally annealed at 950 °C. The obtained sample is referred to as NNO-HMTA.

The second method named "citrates method" uses  $Nd_2O_3$  and metallic Ni as raw materials. In this case, the precursors were dissolved in diluted nitric acid and dried at 80 °C. Citric acid and ethylene glycol dissolved in distilled water were added to the dry nitrates and the mixture was stirred until a transparent solution was obtained. The liquid was slowly evaporated until a polymer was formed. The polymer was fired at 400 °C to eliminate organic products and the remaining powders were heat treated at 950 °C. This sample is referred to as NNO-CIT.

The third preparation method was standard solid state reaction named "SSR method".  $Nd_2O_3$  and NiO were mixed in stoichiometric ratio, ball milled and finally heated at 1200 °C. This sample is referred to as NNO-SSR.

The samples were characterized by X-ray diffraction (XRD) for phase identification and phase purity assessment. XRD analysis was performed with a Philips PW1700 diffractometer with  $\text{CuK}_{\alpha}$  radiations and a graphite monochromator. The morphology and particle size of the so synthesized nickelates were examined by Scanning Electron Microscopy (SEM) using a SEM-FEG Nova Nano SEM 230 microscope.

Chemical compatibility between NNO and CGO electrolyte (Praxair) was checked by XRD on mixtures of NNO-HMTA electrode material and electrolyte powders in a 1:1 weight ratio. The mixture was annealed at 900, 1000 and 1100  $^{\circ}$ C, for 1 h. NNO-HMTA was selected for reactivity test because this sample is the most reactive due to its microstructure [14].

Reactivity between NNO-HMTA and Pt was studied through two types of tests. In one of the tests, NNO powder was spread on a Pt sheet and fired at 900 °C for 72 h. The Pt sheet was afterward observed by SEM in order to detect chemical etching. In the second test, a mixture of NNO-HMTA and Pt powders in a 1:1 weight radio was heated at 700 °C for 72 h. XRD patterns of this mixture were recorded before and after the heat treatment. Similar compatibility tests were performed between an Au sheet and NNO.

The electrochemical characterization of porous NNO electrodes was carried out on dense CGO electrolytes. Symmetrical Au/NNO/CGO/NNO/Au cells were used to study the oxygen electrode mechanism reaction at 0 bias voltage. EIS measurements were performed using a frequency response analyzer (FRA) coupled to an AUTOLAB potentiostat, in the temperature range from 500 up to 750 °C using Ar–O $_2$  mixtures. The resulting spectra were fitted with electrical equivalent circuit using Zview program [19].

Dense CGO electrolytes were prepared by pressing powders and firing them at 1350 °C during 4 h. The relative density of the sintered pellets was higher than 95%. NNO inks were prepared by mixing NNO powders (NNO-HMTA, NNO-CIT and NNO-SSR) with polyvinyl butyral (2% w/w), polyetileneglycol (1% w/w), ethanol (30% w/w) and  $\alpha$ -terpineol (27% w/w). CGO substrates were covered with the NNO ink onto both flat sides by spin coating.

The optimal temperature for promoting electrode adhesion onto CGO was selected from a test performed at 900, 1000 and 1100 °C during 1 h. This test was carried out only for NNO-HMTA sample. The resulting cells were characterized by EIS in synthetic air between 500 and 750 °C and observed by SEM after these measurements. NNO-CIT, NNO-SSR and NNO-HMTA materials were adhered onto CGO electrolytes at 1000 °C for 1 h resulting into electrodes with three different morphologies. The microstructure of top surfaces of the electrodes and NNO/CGO cross sections were examined by SEM. The effect of microstructure on the electrode reaction mechanism was analyzed by EIS under controlled pO2 atmosphere. EIS spectra were collected on symmetrical cells varying pO2 within the range of 10<sup>-4</sup>-1 atm. Controlled pO2 atmospheres were provided by an electrochemical system composed of an oxygen pump and an oxygen sensor using Ar as gas carrier [20].

#### 3. Results and discussion

#### 3.1. Microstructural characterization of NNO powders

Fig. 1 shows SEM images of NNO-HMTA, NNO-CIT and NNO-SSR powders displaying different morphologies. NNO-HMTA shows agglomerates constituted by small submicronic grains with high porosity and poor connectivity (see Fig. 1(a) and (b)).

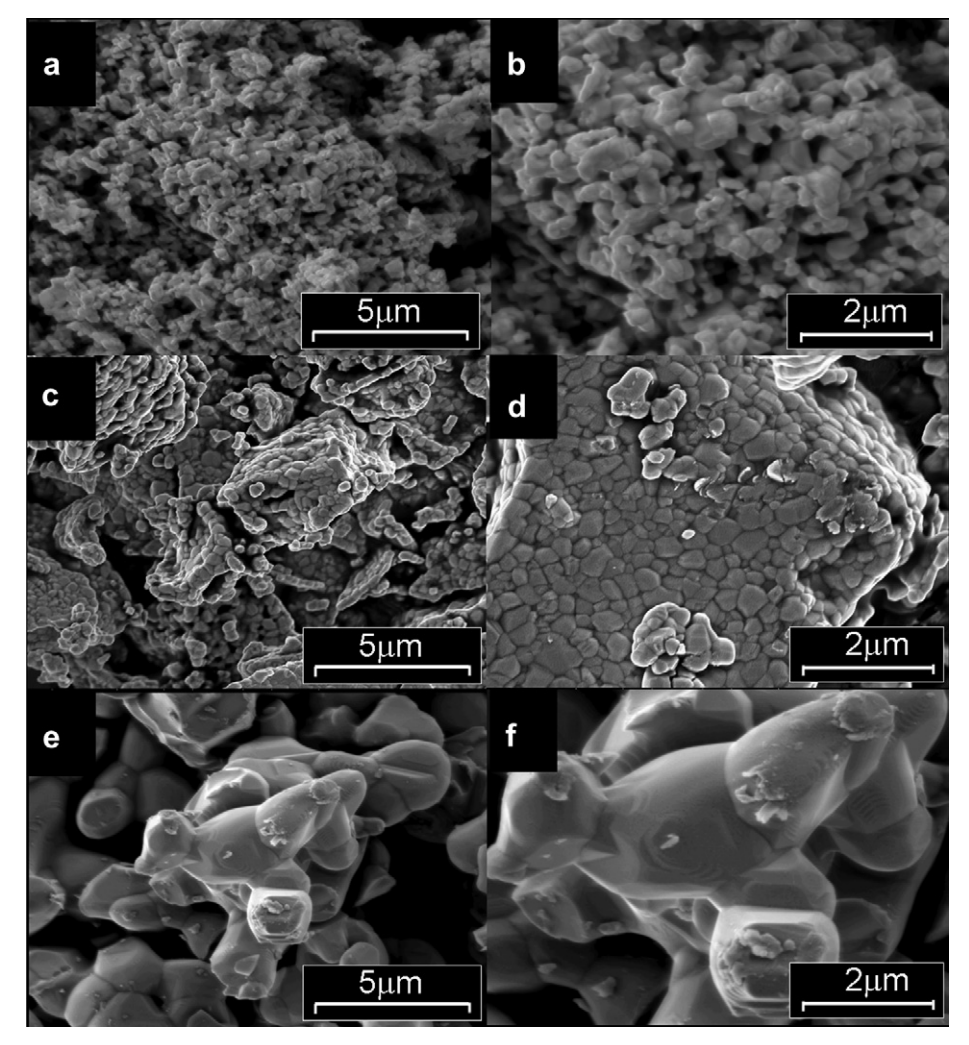


Fig. 1 – SEM images of NNO-HMTA (a) and (b); NNO-CIT (c) and (d); and NNO-SSR (e) and (f) powders.

The NNO-CIT powders present irregular agglomerates with dense surfaces (see Fig. 1(c) and (d)).

As observed in Fig. 1(e) and (f), solid state reaction method produces powder with larger grain size compared to those of HMTA and citrates methods. Hard agglomerates are also visible.

### 3.2. Chemical compatibility

The XRD patterns of the NNO-HMTA and CGO mixture after different treatments are shown in Fig. 2. For the mixtures annealed at 900 and 1000 °C during 1 h, only the diffraction peaks of the starting materials (NNO and CGO) are present. For the mixture treated at 1100 °C for 1 h, additional peaks assigned to the fluorite  $Ce_{1-x}Nd_xO_{(2-x)/2}$  phase are observed [21,22].

Pt is usually used as current collector but chemical reactivity between this metal and  $\rm La_2NiO_4$  has been previously reported [23,24]. In the present work, two chemical compatibility tests of NNO-HMTA with Pt were performed. In Fig. 3, a SEM micrograph of a Pt sheet annealed at 900 °C with NNO-HMTA powder on it, is shown. The zone on which NNO

powder was spread (etched zone) is clearly differentiable from that of clean Pt (clean zone). In order to confirm this reactivity an NNO and Pt powder mixture was heated at 700  $^{\circ}$ C for 22 h. The XRD patterns collected before and after this treatment are shown in Fig. 4. Some unidentified peaks are present in the diffractogram as product of chemical reaction between Pt and NNO

A similar reactivity test between NNO-HMTA and Au sheet was carried out and no reaction was detected (results not shown here). Based on these results, Au mesh was chosen as current collector for EIS experiments.

# 3.3. Electrode microstructure and electrochemical response as a function of T

The optimal temperature for promoting the adhesion of NNO onto CGO was determined by EIS on three NNO-HMTA/CGO/NNO-HMTA cells prepared at 900, 1000 and 1100 °C. As shown in Fig. 5(a), at 900 °C the electrode consists of poor connected particles with a large exposed surface. As the sintering temperature increases, the connectivity among particles increases, leading to a denser microstructure (Fig. 5(c)). In

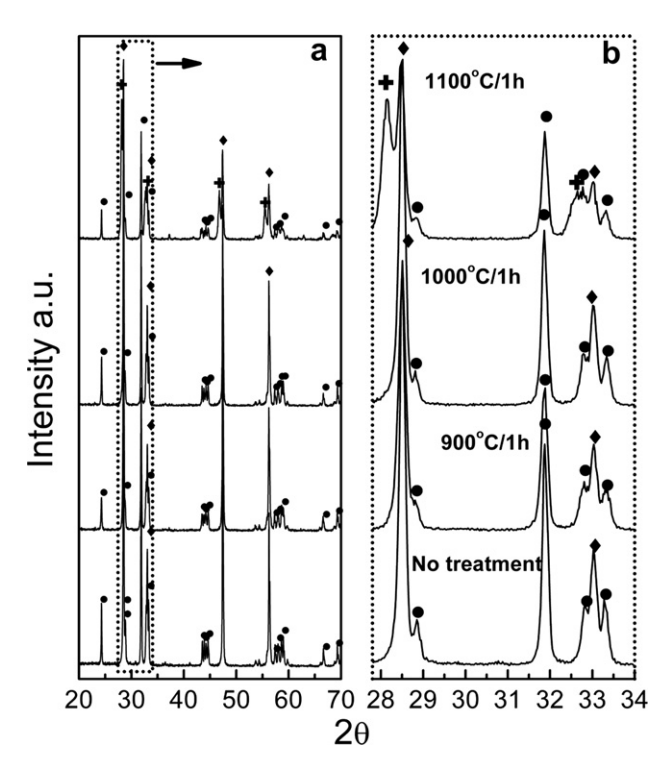


Fig. 2 – XRD patterns of NNO-HMTA and CGO powder mixtures after different heat treatments (a) and zoom in the  $28-34^{\circ}$   $2\theta$  range showing the products of reaction (b). ( $\bullet$ ) Nd<sub>2</sub>NiO<sub>4</sub>, ( $\bullet$ ) CGO, ( $\dagger$ ) Nd<sub>0.5</sub>Ce<sub>0.5</sub>O<sub>1.9</sub>.

the same way, the adhesion of electrode layers onto the electrolyte increases with temperature. Fig. 6 shows that the lowest polarization resistance was obtained upon sintering at 1000 °C. This feature would be related to the well connected particles and relatively good electrode/electrolyte adhesion. At 900 °C, the electrode particles are weakly connected and the adhesion with electrolyte is decreased. Both facts evidently

affect the electrode performance. In the case of the cell sintered at 1100  $^{\circ}$ C, the microstructure is extremely dense. The XRD pattern of the NNO/CGO surface at 1100  $^{\circ}$ C did not show extra peaks. Despite this observation, it is worth to noting that interfacial reaction might not be discarded since reactivity was observed at 1100  $^{\circ}$ C for the powder mixture test (see Section 3.2). This would be one of the reasons for the high polarization resistance values of the cell prepared at 1100  $^{\circ}$ C. In Fig. 6(b) EIS spectra taken at 500  $^{\circ}$ C for the three adhesion temperatures are shown. The minimum electrode polarization resistance was obtained for the cell prepared at 1000  $^{\circ}$ C.

In view of the better performance of the NNO-HMTA/CGO/NNO-HMTA cell prepared at 1000  $^{\circ}$ C, NNO-CIT and NNO-SSR cells were also made at this temperature. Fig. 7 shows SEM images of cross sections of the three NNO/CGO cells after EIS measurements. It can be observed that the adhesion heat treatment at 1000  $^{\circ}$ C for 1 h has not appreciably modified the microstructure of the starting powders. No cracks are present in the three electrodes. This is an expected result, since the thermal expansion coefficients of NNO and CGO are similar [13].

The Arrhenius plot of area specific resistances (ASR) and impedance diagrams, obtained at 550 °C in air for the three cells, are shown in Fig. 8(a) and (b), respectively. NNO-SRR cell exhibits the poorest electrochemical performance. An analysis on the rate-limiting steps of the electrode reaction could shed light to understand the role played by the microstructure on the performance of these materials as oxygen electrodes.

# 3.4. Mechanism of electrode reaction and effect of the microstructure

The oxygen reduction reaction (ORR) of a mixed conductor electrode takes place through several steps: gas phase diffusion, surface adsorption, dissociation of molecular adsorbed oxygen, oxygen incorporation, diffusion inside the electrode and ion transfer across the electrode/electrolyte interface [25]. EIS is a powerful technique for studying the electrode reaction

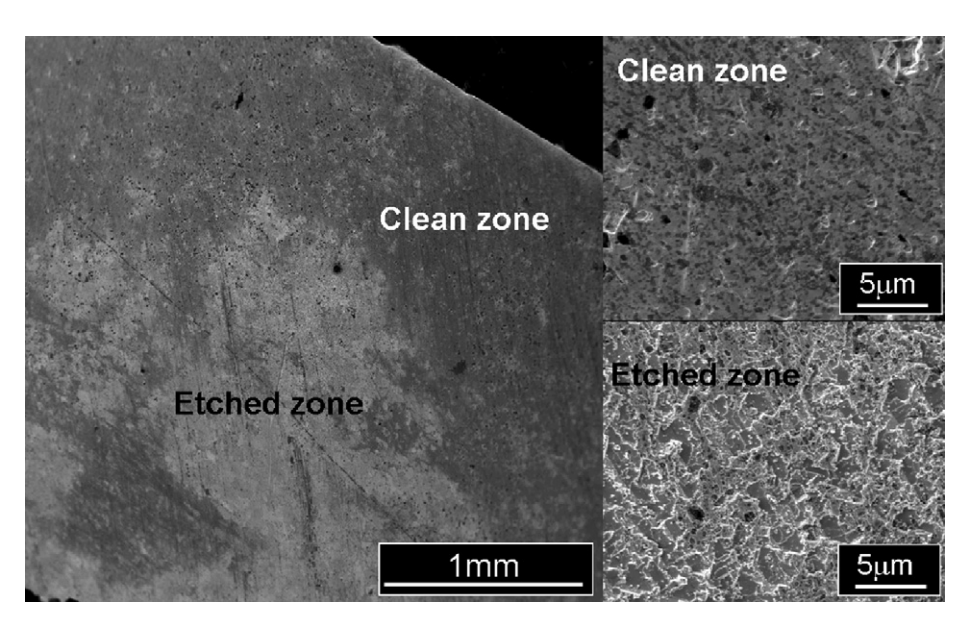


Fig. 3 - SEM images of the surface a Pt sheet after spreading NNO powders on it, and annealing at 900 °C for 72 h.

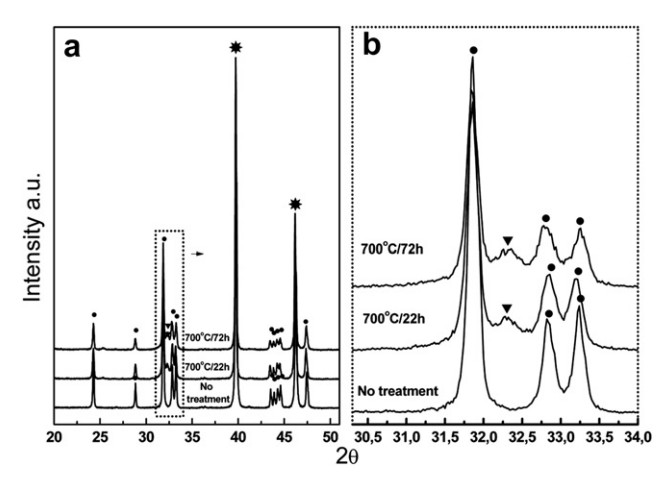


Fig. 4 – XRD patterns of NNO-HMTA and Pt powders mixtures after heat treatment at 700 °C (a) and zoom in the  $30-34^{\circ}$   $2\theta$  range (b). ( $\bullet$ ) Nd<sub>2</sub>NiO<sub>4</sub>, (\*) Pt, ( $\blacktriangledown$ ) unknown.

because it allows to transform a time-scaled process with characteristic relaxation time into a frequency-scaled one.

Two different approaches are currently used to analyze the EIS data. One of them, the approximation proposed by Adler, describes the electrode as a macro homogeneous system and the EIS is the addition of contributions due to a Faradaic process of charge transfer through interfaces and one contribution associated to the convolution of all non-Faradaic processes [26–30]. This approach has been used for modeling the response of electrodes displaying simple Nyquist diagrams. Thus, it is possible to obtain kinetic parameters (equilibrium molar exchange rate and oxygen vacancy diffusion coefficient) [29] from the fit of the EIS diagram. In this modelization, the convolution of non-Faradaic processes is a good approach for those cases in which surface exchange and bulk diffusion dominate.

The other approximation considers a sequential process such as charge transfer, oxygen bulk diffusion, oxygen surface exchange, oxygen adsorption, oxygen gas diffusion etc. The whole impedance is represented by a series of impedance components, each of them describing individual processes  $Z = \sum Z_i$ . This is a helpful approach for those cases where the processes are frequency resolved [31–36].

We have used this last approach to discuss the EIS data since the control of the experimental conditions allowed us to resolve in frequency the different electrode processes.

The frequency response allows to identify different contributions to the electrode process. Thus, in an EIS spectrum each step is characterized by a relaxation frequency, a capacitance and a resistance value. When the relaxation frequencies of the steps are quite different, it is relatively easy to identify each contribution. For each step, under null bias voltage, there is a relation between the polarization resistances and  $pO_2$  values,  $R_p \propto pO_2^{-n}$ , where "n" is characteristic of the nature of the process. Thus, n=1 is related to both, oxygen gas diffusion and no-dissociative adsorption of molecular  $O_2$ , while n=0.5 is associated to dissociative adsorption of O [37]. Besides, it is possible to obtain further information on the nature of electrode process from the capacitance (C) values. Adler indicates that C increases as the dimensionality of the

process increases, changing from  $10^{-6}$  F cm<sup>-2</sup> for doubled layer to 10 F cm<sup>-2</sup> for bulk process [25].

EIS spectra of the three NNO/CGO/NNO cells, recorded at 700 °C in atmospheres with different  $pO_2$  values, are shown in Fig. 9. For the NNO-HMTA and NNO-CIT electrodes, the spectra contain two arcs, suggesting that at least two different rate-limiting steps control the oxygen reduction. For NNO-SSR, the EIS spectra present three arcs in the  $pO_2$  range between 1 and  $8\times 10^{-3}$  atm, and four arcs from  $8\times 10^{-3}$  down to  $5\times 10^{-4}$  atm. Fig. 10 shows the fit of the EIS spectra for the three electrodes at 700 °C under  $pO_2=10^{-3}$  atm and the equivalent circuits used for fitting. In all cases, a resistance  $R_{el}$  in series with an inductance L was included to adjust the effects associated to electrolyte and electrical leads. The symbols in Fig. 10 represent the measured data and the lines are the fitted curves (elementary and overall). Each contribution and its dependency on  $pO_2$  are discussed below.

For NNO-HMTA and NNO-CIT samples the high frequency contributions observed below 600  $^{\circ}$ C, were fitted with RCpe<sub>HF</sub> impedance component composed by a resistance R in parallel with a Constant Phase Element (Cpe), with  $C = 10^{-6} \, \mathrm{F \, cm^{-2}}$ . For NNO-SSR, two high frequency contributions were found at relaxation frequencies of  $10^4$  and  $10^2$  Hz with C of  $10^{-8}$  and 10<sup>-6</sup> F cm<sup>-2</sup>, respectively. The capacitance values C were calculated from eq. (1) where R is the resistance, Q is the pseudo-capacitance, p is an exponent and A is the area of the electrode. These values were obtained from the fitting within Zview program. These arcs are present at up to 700 °C, and their resistances barely vary with pO2. The weak pO2 dependence of these contributions (not shown here) suggests that neither atomic nor molecular oxygen are involved in these rate-limiting steps [38]. Therefore, the high frequency contribution with  $C = 10^{-6} \, \text{F cm}^{-2}$  for all samples could be attributed to oxygen ion transfer from the electrode to the electrolyte [39]. For the NNO-SSR case, the arc with  $C = 10^{-8}$  F cm<sup>-2</sup> should be related to the grain boundary resistance of CGO [40].

$$C = \frac{(R \cdot Q)^{1/p}}{R \cdot A} \tag{1}$$

For all three samples the polarization resistance of the medium frequency ( $R_{\rm MF}$ ) process is the highest, indicating that this process is dominant. The frequency range of this contribution is characteristic of a mechanism controlled by oxygen transport. The Adler approach models phenomena involving oxygen bulk diffusion co-limited with oxygen exchange surface [29]. In the limit in which the oxygen bulk diffusion has control over the oxygen exchange surface, the Adler approach yields to a semi-infinite Warburg-diffusion behavior [29,30] described by the impedance:

$$Z_{W} = \frac{R_{W} tan h\left(\sqrt{i\omega l_{\delta}^{2}/D}\right)}{\sqrt{i\omega l_{\delta}^{2}/D}} \tag{2}$$

with

$$R_W = \frac{l_{\delta}}{\sigma_{\rm ion}}.$$
 (3)

where  $l_{\delta}$  is the characteristic diffusion length and  $\sigma_{\rm ion}$  is the ionic conductivity. In NNO, the ionic conductivity is given by an interstitial oxygen mechanism.

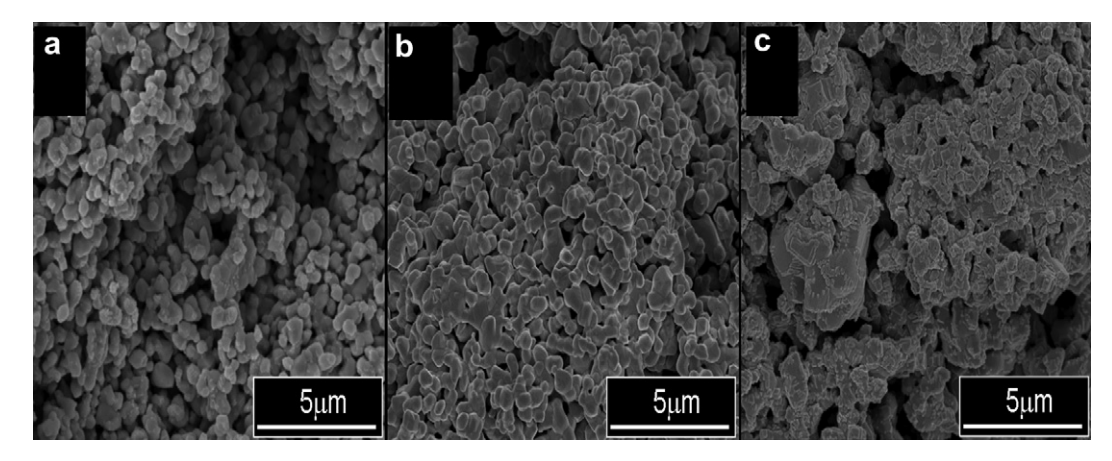


Fig. 5 - SEM images of NNO-HMTA electrode sintered at different temperatures. Top view (a) 900 °C, (b) 1000 °C and (c) 1100 °C.

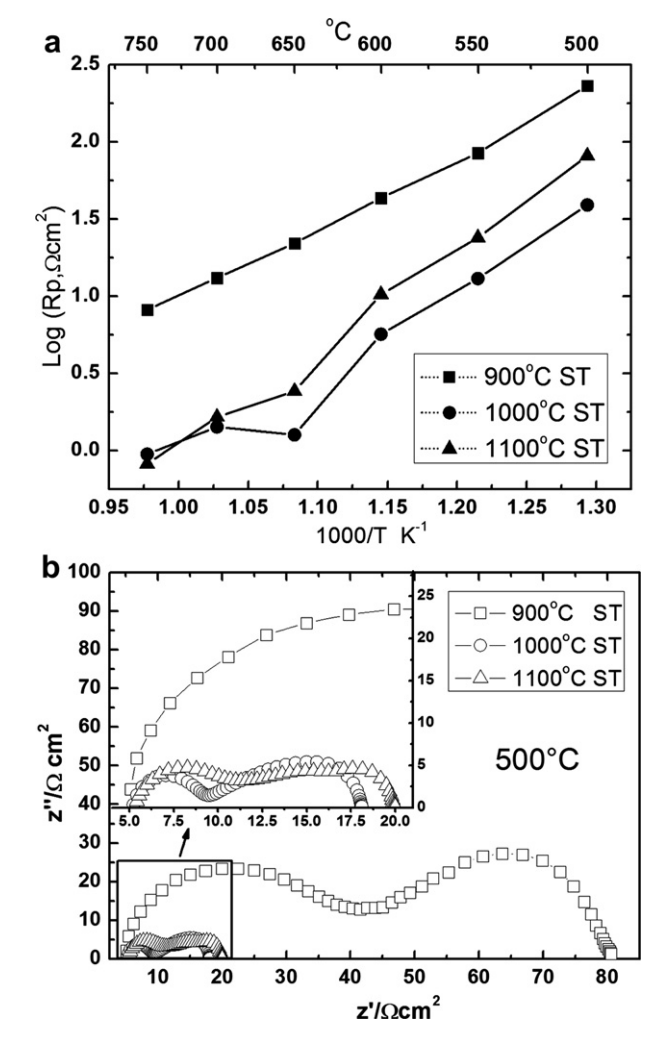


Fig. 6 – (a) Temperature dependence of total ASR and (b) Nyquist plots recorded at 500  $^{\circ}$ C for NNO-HMTA/CGO/NNO-HMTA cells sintered at 900  $^{\circ}$ C, 1000  $^{\circ}$ C and 1100  $^{\circ}$ C (ST: sintering temperature).

Fig. 11(a) shows the dependence of  $\log(R_{\rm MF})$  as a function of  $\log(p{\rm O}_2)$  for all samples at 700 °C, which is noticeably linear. The linear regression gives an n value of 0.15 for NNO-SSR. The n=0.15 is quite close to 1/6, which is the same dependence found for oxygen interstitial defect formation in  ${\rm Ln}_2{\rm NiO}_{4+\delta}$  [10]. Since the ionic conductivity is proportional to the interstitial oxygen concentration, (from eq. (3))  $R_{\rm w}$  would be proportional to  $p{\rm O}_2^{-1/6}$ .

The capacitance values for the Warburg element are calculated from eq. (4), where W-T is the characteristic time of the diffusion and  $R_{\rm w}$  is the resistance of the Warburg. Both parameters are obtained upon fitting the EIS spectra.

$$C = \frac{(W - T)^{1/2}}{R_W} \tag{4}$$

The obtained values of capacitance C, ranging between  $1 \times 10^{-1}$  and  $3 \times 10^{-1}$  F cm<sup>-2</sup>, and n = 0.15, strongly indicate that bulk diffusion of interstitial O is the rate-limiting step in the medium frequency range for NNO-SSR sample.

An n=0.25 (see Fig. 11(a)) and C values ranging between  $3\times 10^{-2}-6\times 10^{-1}$  and  $9\times 10^{-2}-1\times 10^{-1}$  F cm<sup>-2</sup> were determined for NNO-CIT and NNO-HMTA electrodes, respectively. This dependence on  $pO_2$  is normally attributed to electron transfer process, also called "oxygen surface exchange" [37]. Besides, C values within the range  $10^{-3}-10^{-2}$  F cm<sup>-2</sup> are representative of surface processes [25]. These results suggest a major contribution of surface processes in the control of oxygen transport for NNO-CIT and NNO-HMTA electrodes. A similar behavior was found for another Ruddlesden–Popper phase,  $Sr_3FeMO_{6+\delta}$  (M = Fe, Co, Ni), studied as cathode for SOFC [36].

The different observed rate-limiting steps between NNO-HMTA, NNO-CIT and NNO-SSR should be related to a grain size effect. SEM micrographs indicate an average grain size about 200 nm and 250 nm for NNO-HMTA and NNO-CIT samples, respectively. The grain size values are one order of magnitude higher for NNO-SSR, around 2  $\mu m$ . These different microstructures should be the cause of a competition between oxygen surface exchange and interstitial oxygen diffusion.

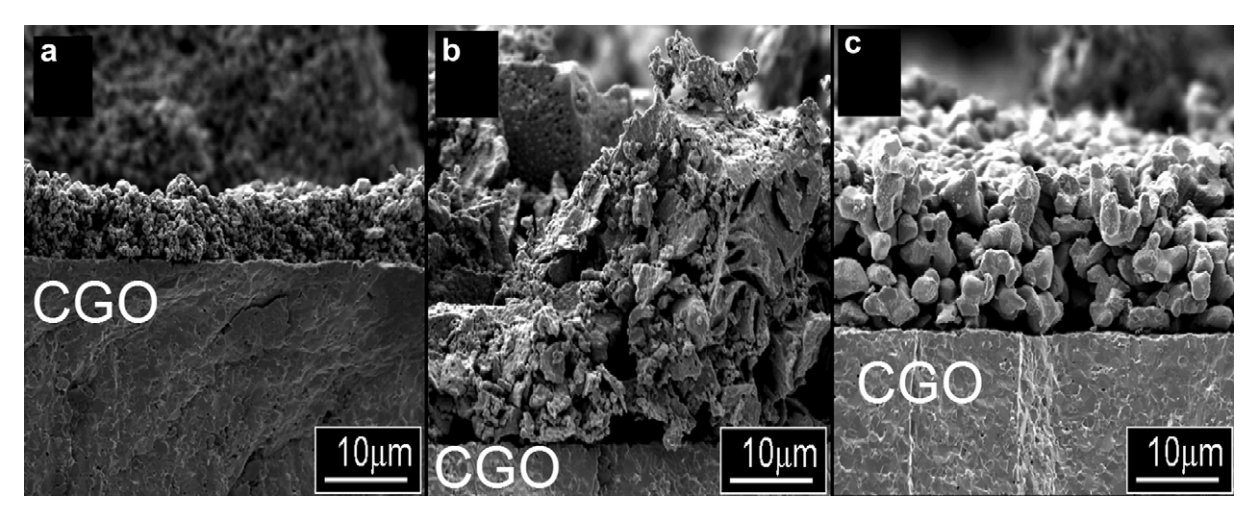


Fig. 7 — SEM micrographs of cross sections of electrode/electrolyte interfaces for (a) NNO-HMTA, (b) NNO-CIT and (c) NNO-SSR electrodes on CGO substrates after EIS measurements.

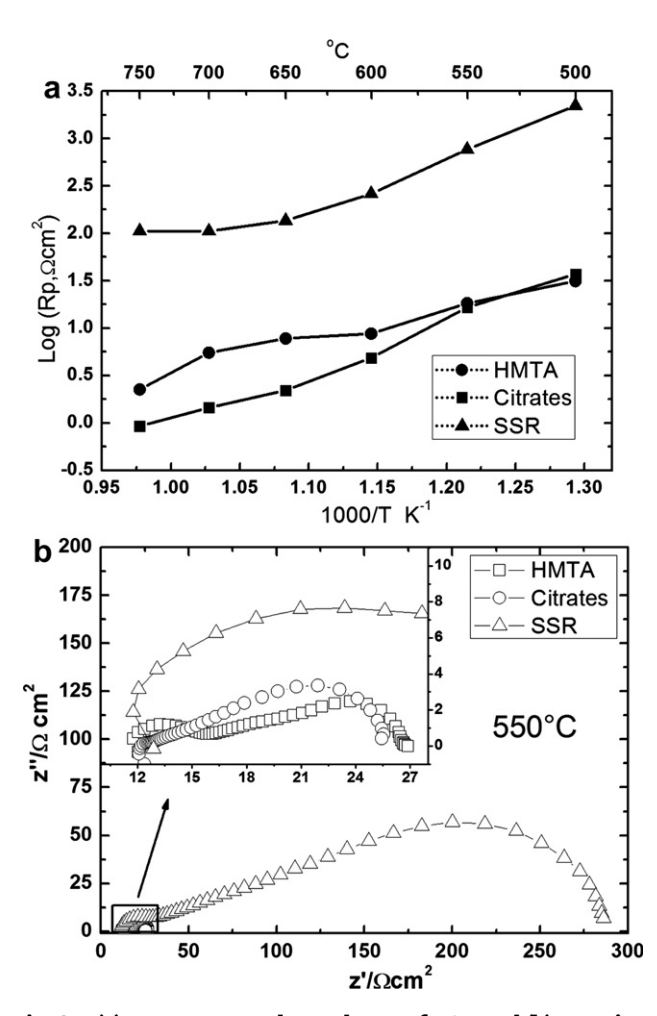


Fig. 8 – (a) Temperature dependence of ASR and (b) Nyquist plots recorded at 550  $^{\circ}$ C for NNO-HMTA/CGO/NNO-HMTA, NNO-CIT/CGO/NNO-CIT and NNO-SSR/CGO/NNO-SSR cells in air.

The ratio between the oxygen diffusion coefficient " $D_{\rm chem}$ " and the oxygen exchange coefficient " $k_{\rm chem}$ " determined either by conductivity relaxation measurements or the equivalent from tracer experiment with SIMS, defines a characteristic length  $Lc = D_{\rm chem}/k_{\rm chem} = D^*/k^*$ . The comparison between "Lc" and a characteristic length of the electrode "Lp" allows for the discussion of whether the oxygen transport in NNO is limited by surface exchange or by bulk diffusion. Thus, when Lp < Lc the oxygen transport is controlled by surface exchange and therefore the entire surface of the electrode is active. For Lp > Lc, the oxygen incorporation is controlled by bulk diffusion and mainly occurs close to the Triple Phase Boundary (TPB) [30].

For NNO, quite different Lc values have been determined either using conductivity relaxation measurements  $Lc = D_{chem}/K_{chem} = 4 \mu m$  [41] or isotopic exchange  $Lc = D^*/$  $K^* = 170 \,\mu\text{m}$  [4]. A rough estimation of Lp could be made from SEM images. For NNO-HMTA and NNO-SSR Lp could be assigned to the particle radii, 100 nm and 1 µm, respectively. For NNO-CIT the presence of dense agglomerates make the determination of Lp more difficult. Thus, if Lp is assigned to the radii of particles, Lp would be ~100 nm, whereas considering agglomerates Lp would be ~3 μm. Nevertheless, these Lp values are lower than those Lc discussed before, which would suggest surface exchange control for oxygen transport in the three electrodes. However, our polarization resistance data for the medium frequency contribution indicate surface control by oxygen incorporation (n = 1/4) for NNO-HMTA/CGO and NNO-CIT/CGO and pure diffusion control (n = 1/6) for NNO-SSR/CGO. This disagreement might be caused by the high uncertainties on both, the determination of Lc and the evaluation of Lp. The comparison between Lc and Lp makes sense for electrodes with well defined geometries (rods, dense layers, spherical and monodisperse particles, etc.). However, for our electrodes, other microstructure factors such as particle size distribution, particle connectivity, contact angle, irregular shape of precipitates, etc. could strongly affect the oxygen transport behavior [25].

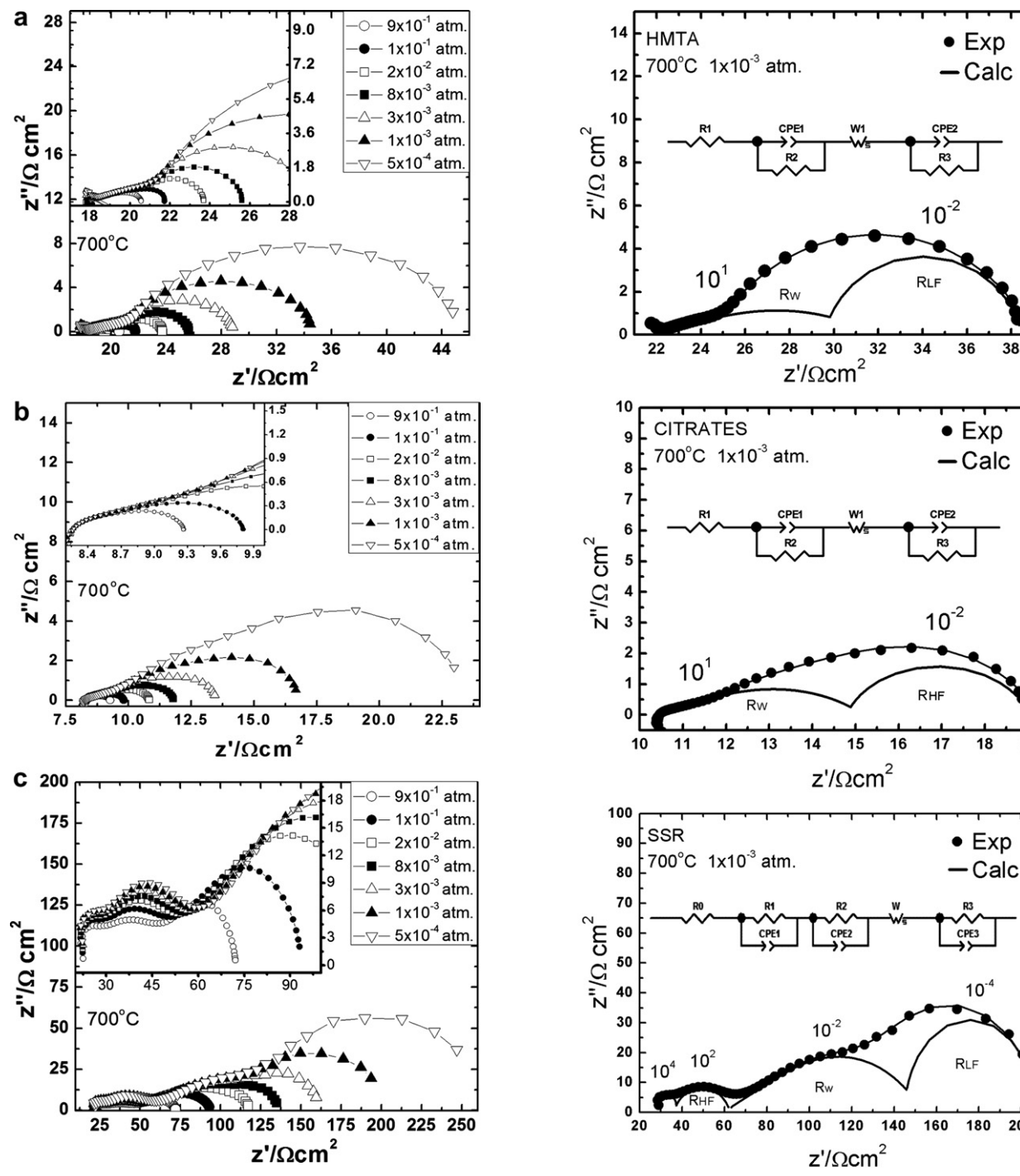
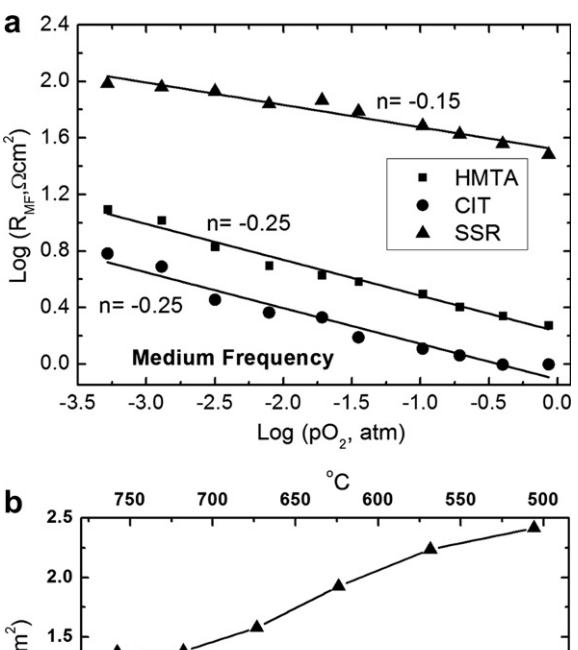


Fig. 9 — Nyquist impedance curves for NNO electrodes obtained by NNO-HMTA (a), NNO-CIT (b) and NNO-SSR (c) methods. Measurements performed at different  $pO_2$  using Ar as carrier gas at 700 °C.

Fig. 10 – EIS spectra for NNO-HMTA, NNO-CIT and NNO-SSR at 700 °C and  $pO_2 = 1 \times 10^{-4}$  atm. The lines correspond to the fitting result with an equivalent circuit.

Egger et al. have also performed a comparative study of oxygen exchange kinetics between  $Nd_2NiO_{4+\delta}$  and  $La_{0.6}Sr_{0.4}CoO_{3-\delta}$  by conductivity relaxation measurements [41]. They obtained at 700 °C similar Lc values for both oxides. However, previous studies on cobaltites indicate that no rate-limiting step by surface control was observed for electrodes with quite different geometries, obtained either from powders

[35] or sputtered films [42]. The microstructure of powders of reference [33] is similar to that of our NNO-HMTA samples. Given the similar Lc values for  $Nd_2NiO_{4+\delta}$  and  $La_{0.6}Sr_{0.4}CoO_{3-\delta}$ , a similar rate-limiting step should be expected. Therefore, we consider that a different source should be responsible for the variation of the limiting mechanism observed for NNO-HMTA and NNO-CIT respect to that of NNO-SSR sample.



2.0

EBO 1.5

Nedium Frequency

0.0

0.5

0.95

1.00

1.05

1.10

1.15

1.20

1.25

1.30

1000/T K<sup>-1</sup>

Fig. 11 - (a) ASR versus  $pO_2$  at 700  $^{\circ}$ C using a double-logarithmic representation, (b) comparison of Arrhenius plots of the polarization resistance for medium frequency contribution of NNO-HMTA, NNO-CIT and NNO-SSR electrodes.

Although no reactivity between NNO and CGO was observed by XRD after the adhesion treatment, at 1000 °C for 1 h, the presence of reaction products in low concentrations cannot be discarded. Reaction products either at the nanometric scale or of amorphous nature, could be undetectable by XRD. It should be noted that reactivity between NNO and CGO was detected by XRD after 72 h at 1000 °C [14]. These reaction products would extend from the NNO/CGO interface to the TPB and beyond it, to the gas/electrode interface located near the TPB (see Fig. 12). The impurities formed as a consequence of reactivity between NNO and CGO could affect both, surface and interface processes. However, in our samples, an increment on the ionic transfer resistance due to this effect was not observed.

As we reported before, the chemical reactivity with CGO is strongly dependent on the microstructure [14] and its influence on the electrochemical performance should be major for NNO-CIT and NNO-HMTA samples than for NNO-SSR. Similar results on the rate-limiting steps were found by Zhou et al. while studying A-site deficient  $(Ba_{0.5}Sr_{0.5})_{1-x}Co_{0.8}Fe_{0.2}O_{3-\delta}$  perovskites as electrodes on Samarium Doped Ceria (SDC)

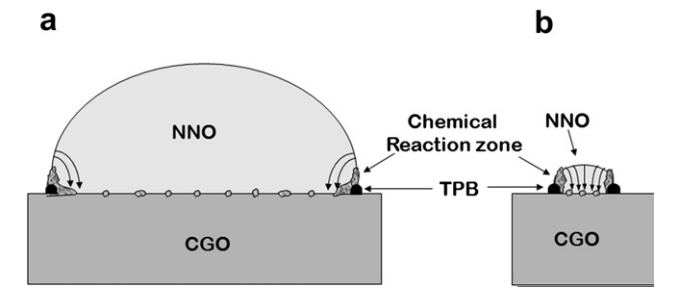


Fig. 12 — Schematic representation of chemical reaction zone in electrode/electrolyte interface (a) micrometric particles size (NNO-SSR). (b) Submicronic particles size (NNO-GIT and NNO-MTA). The arrows suggest the effective diffusion path.

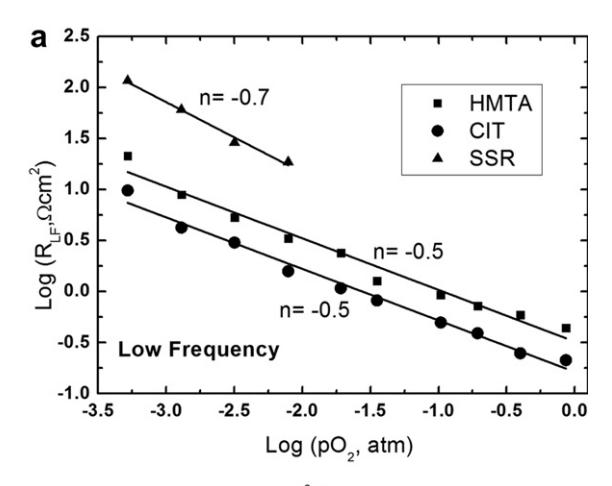
electrolyte. They observed an n=0.25 for the dependence of the polarization resistance with  $pO_2$  and C values between  $2\times 10^{-2}$  and  $5\times 10^{-2}$  F cm<sup>-2</sup>, which has been attributed to the electron transfer step of oxygen reduction [43]. The polarization resistances of these  $(Ba_{0.5}Sr_{0.5})_{1-x}Co_{0.8}Fe_{0.2}O_{3-\delta}$  compounds associated to this step, increase as the A-site deficiency increases. This increment is likely due to impurities formed at the TPB [43].

In Fig. 12(a) and (b) it is shown a schematic comparison of a micronic (NNO-SSR) and submicronic (NNO-HMTA, NNO-CIT) grain on a CGO electrolyte, respectively. The reaction zone is similar in both cases, but the ratio between reacted and unreacted zones is clearly larger for smaller grains. In the case of our NNO-SSR electrodes, although reactivity at the TPB and the surrounding region should exist, the size of the reacted region that extends beyond the TPB, would be appreciably smaller as compared to the particle size (see Fig. 12(a)). However, for smaller particles (as it is the case of the NNO-HMTA and the NNO-CIT electrodes) the extension of the reaction zone compared to the particle size should be appreciably larger than those of NNO-SSR (see Fig. 12(b)). The ratio between the reaction zone and the particle size seems to be determinant for the mechanism controlling the oxygen electrode reaction at medium frequencies. Despite this, Fig. 11(b) shows a larger resistance for NNO-SSR than NNO-HMTA and NNO-CIT in the whole temperature range. The reason for this should be the lower effective diffusion region of NNO-HMTA and NNO-CIT rather than that of NNO-SSR, which improves the diffusion process (see Fig. 12).

The low frequency contribution, which becomes significant at higher temperatures and low  $pO_2$  values, was fitted with an RCpe<sub>LF</sub> impedance component composed by a resistance R in parallel with a Cpe component. For NNO-HMTA and NNO-CIT, the n=0.5 (see Fig. 13(a)) together with C around  $10^{-2}$  F cm<sup>-2</sup>, suggests a rate-limiting step by dissociative adsorption [44,45].

When the dissociative adsorption/desorption process  $(O_2 + 2S \mathop{\rightleftharpoons} 2O_{ad})$  is the rate-limiting step, the impedance is mathematically equivalent to the impedance of the parallel circuit of R and C with a polarization resistance given by:

$$R_{\rm ads} = \frac{R1}{4F^2 A C_{\rm s} \theta^{\rm eq}} \tag{5}$$



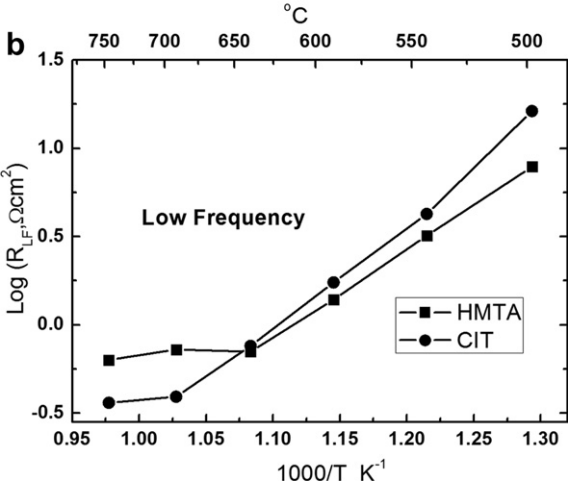


Fig. 13 - (a) Polarization resistance versus pO $_2$  at 700  $^{\circ}$ C, using a double-logarithmic representation, (b) comparison of Arrhenius plots of the polarization resistance for low frequency contribution of NNO-HMTA, NNO-CIT and NNO-SSR electrodes.

where  $A=2\overrightarrow{k_s}p_{O_2}(1-\theta^{eq})+2\overrightarrow{k_s},\theta^{eq}/C_s$ ,  $C_s$  is the concentration of adsorption site, and  $k_s$  and  $k_s$  are the adsorption desorption coefficients, respectively. Considering Langmuir isotherm of adsorption in the limit of low coverage  $\theta^{eq}\approx Kp_{O_2}^{1/2}$ , a dependence of  $R_{ads}\propto p_{O_2}^{-1/2}$  is found [45–47], in agreement with our low frequency result for NNO-CIT and NNO-HMTA.

At temperatures below 600 °C in air, for NNO-HMTA electrode, the polarization resistance of this contribution is lower than that of NNO-CIT (see Fig. 13(b)). This may be due to the fact that at these temperatures, the adsorption process is the most relevant contribution. The absorption process would be enhanced for NNO-HMTA due to its high active surface (see Fig. 1).

For NNO-SSR sample, the low frequency contribution is observed only at  $pO_2$  range between  $8 \times 10^{-3}$  and  $5 \times 10^{-4}$  atm and the resistance values vary with  $pO_2^{-0.7}$  (see Fig. 13(a)). The C values are around  $10^{-1}$  F cm<sup>-2</sup>, which are between those associated to  $O_2$  gas diffusion into the porous electrode (n=1) and dissociative adsorption process (n=0.5). This intermediate n value should suppose a rate-limiting step given by a convolution of dissociative adsorption and gaseous diffusion as

observed by other authors [35]. It is probable that the dissociative adsorption process has been always present for the NNO-SSR sample at other temperatures and higher  $pO_2$  values. This process could not be differentiated because it was masked by the large Warburg-diffusion contribution. As shown in Fig. 10(c), the NNO-SSR diffusion contribution is present in the frequency range  $10^{-1}$ – $10^{-3}$  Hz, while the dissociative adsorption is observed within  $10^{-1}$ – $10^{-2}$  Hz for NNO-HMTA and NNO-CIT samples (Fig. 10(a) and (b)). The appearance of  $O_2$  gas diffusion process as rate-limiting step, only for NNO-SSR sample, could be due to its dense microstructure and low porosity as compared with NNO-HMTA and NNO-CIT.

#### 4. Conclusions

Three different synthesis routes (HMTA, Citrates and SSR) yielded to  $Nd_2NiO_{4+\delta}$  powders with different microstructures.

The heat treatment for electrode adhesion on CGO electrolyte was optimized within the 900–1100 °C range, in order to get the minimum polarization resistance.

The EIS spectra showed for the three electrodes were well frequency resolved with three main frequency ranges: high, medium and low.

For the high frequency range the rate-limiting step was associated to oxygen ion transfer electrode/electrolyte, while for the medium frequency range the microstructure and reactivity seem to determine the rate-limiting step. For NNO-SSR the rate-limiting step at medium frequency range is due to oxygen bulk diffusion whereas for NNO-HMTA and NNO-CIT materials the surface oxygen exchange controls the oxygen transport through the electrode.

The microstructure also plays a role on the limiting mechanism in the low frequency range which has been identified as dissociative adsorption in samples with small particle sizes and high porosity (NNO-HTMA and NNO-CIT) and a convolution of processes of adsorption and gas diffusion in the sample with dense microstructure and low porosity (NNO-SSR).

The microstructure plays a crucial role not only on the values of polarization resistance but also on the operating mechanism mainly in the medium frequency range. Reactivity between NNO and CGO which seems to be present but not detected by XRD, would affect mostly the NNO-HTMA and NNO-CIT electrodes, determining in this way the rate-limiting step.

Reactivity between NNO and CGO is an important drawback for the use of NNO as electrode materials on CGO electrolytes.

#### Acknowledgments

This work was supported by CNEA (Argentine Atomic Energy Commission), CONICET (Argentine Research Council), UNCuyo and ANPCyT. The authors thank Mr. C. Cotaro for his technical assistance in SEM observations. We also thank Ph.D. A. Soldati, MSc. J. Vega-Castillo and Miss M.C. Ferreiro for discussions and English revision of this manuscript.

#### REFERENCES

- Laguna-Bercero MA. Recent advances in high temperature electrolysis using solid oxide fuel cells: a review. J Power Sources 2012;203:4

  –16.
- [2] Brisse A, Schefold J, Zahid M. High temperature water electrolysis in solid oxide cells. Int J Hydrogen Energy 2008; 33:5375—82.
- [3] Jensen S, Larsen P, Mogensen M. Hydrogen and synthetic fuel production from renewable energy sources. Int J Hydrogen Energy 2007;32:3253-7.
- [4] Mauvy F, Bassat JM, Boehm E, Manaud JP, Dordor P, Grenier JC. Oxygen electrode reaction on Nd<sub>2</sub>NiO<sub>4+δ</sub> cathode materials: impedance spectroscopy study. Solid State Ion 2003;158:17–28.
- [5] Wan J, Goodenough JB, Zhu JH.  $Nd_{2-x}La_xNiO_{4+\delta}$ , a mixed ionic/electronic conductor with interstitial oxygen, as a cathode material. Solid State Ion 2007;178:281–6.
- [6] Chauveau F, Mougin J, Mauvy F, Bassat JM, Grenier JC. Development and operation of alternative oxygen electrode materials for hydrogen production by high temperature steam electrolysis. Int J Hydrogen Energy 2011;3(6):7785–90.
- [7] Chauveau F, Mougin J, Bassat JM, Mauvy F, Grenier JC. A new anode material for solid oxide electrolyser: the neodymium nickelate Nd<sub>2</sub>NiO<sub>4+δ</sub>. J Power Sources 2010;195:744–9.
- [8] Naumovich E, Patrakeeva M, Kharton V, Yaremchenko A, Logvinovich D, Marques F. Oxygen nonstoichiometry in  $La_2Ni(M)O_{4+\delta}$  (M = Cu, Co) under oxidizing conditions. Solid State Sci 2005;7:1353–62.
- [9] Skinner S. Characterization of  ${\rm La_2NiO_{4+\delta}}$  using in-situ high temperature neutron powder diffraction. Solid State Sci 2003; 5:419–26.
- [10] Kharton V, Viskup A, Kovalevsky A, Naumovich E, Marques F. Ionic transport in oxygen-hyperstoichiometric phases with K<sub>2</sub>NiF<sub>4</sub>-type structure. Solid State Ion 2001;143:337–53.
- [11] Minervini L, Grimes R, Kilner J, Sickafus K. Oxygen migration in La<sub>2</sub>NiO<sub>4+ô</sub>. J Mater Chem 2000;10:2349–54.
- [12] Skinner SJ, Kilner JA. Oxygen diffusion and surface exchange in  $La_{2-x}Sr_xNiO_{4+\delta}$ . Solid State Ion 2000;135:709–12.
- [13] Boehm E, Bassat JM, Dordor P, Mauvy F, Grenier JC, Stevens P. Oxygen diffusion and transport properties in nonstoichiometric  ${\rm Ln_{2-x}NiO_{4+\delta}}$  oxides. Solid State Ion 2005;176:2717–25.
- [14] Montenegro-Hernández A, Vega-Castillo J, Mogni L, Caneiro A. Thermal stability of Ln<sub>2</sub>NiO<sub>4+δ</sub> (Ln: La, Pr, Nd) and their chemical compatibility with YSZ and CGO solid electrolytes. Int J Hydrogen Energy 2011;36:15704–14.
- [15] Mauvy F, Lalanne C, Bassat JM, Grenier JC, Zhao H, Huo L, et al. Electrode properties of  $Ln_2NiO_{4+\delta}$  (Ln = La, Nd, Pr) AC impedance and DC polarization studies. J Electrochem Soc 2006;153(8):1547–53.
- [16] Baqué L, Djurado E, Rossignol C, Marinh D, Caneiro A, Serquis A. Electrochemical performance of nanostructured IT-SOFC cathodes with different morphologies. ECS Trans 2009;25(2):2473–80.
- [17] Zhao K, Xu Q, Huang D-P, Chen M, Kim B-H. Microstructure and electrode properties of  $La_{0.6}Sr_{0.4}Co_{0.2}Fe_{0.8}O_{3-\delta}$  spin-coated on  $Ce_{0.8}Sm_{0.2}O_{2-\delta}$  electrolyte. Ionics 2011;17(3):247–54.
- [18] Baqué L, Caneiro A, Moreno MS, Serquis A. High performance nanostructured IT-SOFC cathodes prepared by novel chemical method. Electrochem Commun 2008;10:1905—8.
- [19] Johnson D. Zview version 2.9b. Scribner Associates, Inc.; Copyright 1990—1995.
- [20] Caneiro A, Bavdaz P, Fouletier J, Abriata JP. Adaptation of an electrochemical system for measurement and regulation of oxygen partial pressure to a symmetrical thermogravimetric analysis system developed using a Cahn 1000 electrobalance. Rev Sci Instrum 1982;53:1072-5.

- [21] Stephens IEL, Kilner JA. Ionic conductivity of  $Ce_{1-x}Nd_xO_{2-x/2}$ . Solid State Ion 2006;177:669–76.
- [22] Chavan SV, Mathews MD, Tyagi AK. Phase relations and thermal expansion studies in the  $CeO_2$ -Nd<sub>O1.5</sub> system. Mater Res Bull 2005;40:1558–68.
- [23] Montenegro-Hernández A, Mogni L, Caneiro A. La<sub>2</sub>NiO<sub>4+ $\delta$ </sub> as cathode for SOFC: reactivity study with YSZ and CGO electrolytes. Int J Hydrogen Energy 2010;35(11):6031–6.
- [24] Sayers R, Skinner SJ. Evidence for the catalytic oxidation of La<sub>2</sub>NiO<sub>4+δ</sub>. J Mat Chem 2011;21:414–9.
- [25] Adler SB. Factors governing oxygen reduction in solid oxide fuel cell cathodes. Chem Rev 2004;104:4791–843.
- [26] Adler SB. Electrode kinetics of porous mixed-conducting oxygen electrodes. J Electrochem Soc 1996;143(11):3554–64.
- [27] Kreller CR, Drake ME, Adler SB. Influence of electrode morphology on electrochemical response of SOFC cathodes. ECS Trans 2010;28(11):105–21.
- [28] Kreller CR, Drake ME, Adler SB, Chen H-Y, Yu H-C, Thornton K, et al. Modeling SOFC cathodes based on 3-D representations of electrode microstructure. ECS Trans 2011;35(1):815—22.
- [29] Lu Y, Kreller C, Adler SB. Measurement and modeling of the impedance characteristics of porous  $\text{La}_{1-x}\text{Sr}_x\text{CoO}_{3-\delta}$  electrodes. J Electrochem Soc 2009;156(4):B513–25.
- [30] Fleig J, Maier J. The polarization of mixed conducting SOFC cathodes: effects of surface reaction coefficient, ionic conductivity and geometry. J Eur Ceram Soc 2004;24:1343-7.
- [31] Jensen SH, Hauch A, Hendriksen PV, Mogensen M, Bonanos N, Jacobsen T. A method to separate process contributions in impedance spectra by variation of test conditions. J Electrochem Soc 2007;154(12):B1325-30.
- [32] Wang Y, Zhang L, Chen F, Xia C. Effects of doped ceria conductivity on the performance of  $La_{0.6}Sr_{0.4}Co_{0.2}Fe_{0.8}O_{3-\delta}$  cathode for solid oxide fuel cell. Int J Hydrogen Energy 2012; 37:8582–91.
- [33] Esquirol A, Brandon NP, Kilner JA, Mogensen M. Electrochemical characterization of La<sub>0.6</sub>Sr<sub>0.4</sub>Co<sub>0.2</sub>Fe<sub>0.8</sub>O<sub>3</sub> cathodes for intermediate-temperature SOFCs. J Electrochem Soc 2004;151(11):A1847-55.
- [34] Magnone M, Miyayama M, Traversa E. Electrochemical impedance spectroscopy analysis of  $Pr_{0.8}Sr_{0.2}Co_{0.5}Fe_{0.5}O_{3-\delta}$  as cathode material for intermediate temperature solid oxide fuel cells. J Electrochem Soc 2010;157(3):B357–64.
- [35] Grunbaum N, Dessemond L, Fouletier J, Prado F, Mogni L, Caneiro A. Rate limiting steps of the porous  $La_{0.6}Sr_{0.4}Co_{0.8}Fe_{0.2}O_{3-\delta}$  electrode material. Solid State Ion 2009;180(28–31):1448–52.
- [36] Mogni L, Grunbaum N, Prado F, Caneiro A. Oxygen reduction reaction on Ruddlesden-Popper phases studied by impedance spectroscopy. J Electrochem Soc 2011;158(2): B202-7.
- [37] Takeda Y, Kanno R, Noda M, Tomida Y, Yamamoto O. Cathodic polarization phenomena of perovskite oxide electrodes with stabilized zirconio. J Electrochem Soc 1987;134(11):2656–61.
- [38] Kim JD, Kim GD, Moon JW, Park YI, Lee WH, Kobayashi K, et al. Characterization of LSM-YSZ composite electrode by ac impedance spectroscopy. Solid State Ion 2001;143:379–89.
- [39] Baumann FS, Fleig J, Habermeier HU, Maier J. Ba<sub>0.5</sub>Sr<sub>0.5</sub>Co<sub>0.8</sub>Fe<sub>0.2</sub>O<sub>3-δ</sub> thin film microelectrodes investigated by impedance spectroscopy. Solid State Ion 2006;177: 3187–91, http://www.sciencedirect.com/science/article/pii/ S0167273806004383-aff1.
- [40] Dusastre V, Kilner JA. Optimisation of composite cathodes for intermediate temperature SOFC applications. Solid State Ion 1999;126:163–74.
- [41] Egger A, Bucher E, Sitte W. Oxygen exchange kinetics of the IT-SOFC cathode material.  $Nd_2NiO_{4+\delta}$  and comparison with  $La_{0.6}Sr_{0.4}CoO_{3-\delta}$ . J Electrochem Soc 2011;158(5):B573—9.

- [42] Ringuede A, Fouletier J. Oxygen reaction on strontium-doped lanthanum cobaltite dense electrodes at intermediate temperatures. Solid State Ion 2001;139:167–77.
- [43] Zhou W, Ran R, Shao Z, Jin W, Xu N. Evaluation of A-site cation-deficient (Ba $_{0.5}$ Sr $_{0.5}$ ) $_{1-x}$ Co $_{0.8}$ Fe $_{0.2}$ O $_{3-\delta}$  (x>0) perovskite as a solid-oxide fuel cell cathode. J Power Sources 2008;182: 24–31.
- [44] Siebert E, Hammouche A, Kleitz M. Impedance spectroscopy analysis of La<sub>1-x</sub>Sr<sub>x</sub>MnO<sub>3</sub> yttria-stabilized zirconia electrode kinetics. Electrochem Acta 1995;40:1741–53.
- [45] Fukunaga H, Koyama M, Takahashi N, Wen C, Yamada K. Reaction model of dense  $\rm Sm_{0.5}Sr_{0.5}CoO_3$  as SOFC cathode. Solid State Ion 2000;132:279-85.
- [46] Koyama M, Wen C-J, Masuyama T, Otomo J, Fukunaga H, Yamada K, et al. The mechanism of porous Sm<sub>0.5</sub>Sr<sub>0.5</sub>CoO<sub>3</sub> cathode used in solid oxide fuel cells. J Electrochem Soc 2001; 148(7):A795–801.
- [47] Endo A, Fukunaga H, Wen C, Yamada K. Cathodic reaction mechanism of dense La<sub>0.6</sub>Sr<sub>0.4</sub>CoO<sub>3</sub> and La<sub>0.81</sub>Sr<sub>0.09</sub>MnO<sub>3</sub> electrodes for solid oxide fuel cells. Solid State Ion 2000;135:353–8.